PAPER

Check for updates

Unsubstituted thiophene−diketopyrrolopyrrole conjugated polymer thin films *via* oxidative chemical vapor deposition − electronic behavior†

Marek K. Charyton, [ID] [a] Tobias Reiker, [bc] Kamil Kotwica, [ID] [de] Monika Góra, [f] Helmut Zacharias [ID] [b] and Nicolas D. Boscher [ID] ∗[a]

Conjugated polymers (CPs) based on diketopyrrolopyrrole (DPP) constitue an important class of high-performance organic semiconductors. While *N*-alkylation of DPP is required for the solution-based synthesis of DPP-based CPs, oxidative chemical vapour deposition (oCVD) is shown to provide a straightforward solventless and scalable approach for the facile polymerisation of *N*-unsubstituted DPP. The oCVD reaction of 3,6-di(2-thienyl)-2,5-dihydropyrrolo[3,4-*c*]pyrrole-1,4-dione (TDPP) yields polymer thin films combining H-bonding and conjugated covalent bonds, resulting in a superior conductivity and a systematic increase of the lifetime of electronically excited states compared to *N*-alkylated counterparts.

Introduction

Serendipitously discovered in 1974,[1] diketopyrrolopyrrole (DPP) rapidly reached commercialization as high-performance pigments for paints, inks and plastics (*e.g.* Ferrari red pigment). Beyond their intense coloration and wide range of colour shade,[2,3] the industrial and commercial success of DPP derivatives was mainly dictated by their low fabrication costs, low dissolvability and excellent thermal[2] and photo-stability (8th-grade light fastness).[4–6] For example, DPP pigments based on a DPP core flanked by two aromatic moieties can readily be produced from the reaction of inexpensive aromatic nitriles with succinic acid ester.[4] Along the past decade, DPPs have also attracted a growing interest for organic electronic,[7] photo-voltaic[7,8] and photoelectrocatalytic applications[9] due to their intrinsic physical and chemical properties. DPPs' properties are strongly influenced by the substituents attached to the core (*e.g.* phenyl, pyridyl, thienyl, furanyl, seleneyl)[10] and *N*-positions (mainly alkyl groups). DPPs can either be used as single molecules, *e.g.* photosensitizers on metal oxide surfaces,[9] or (co)polymerised,

e.g. p-type, n-type or ambipolar polymeric semiconductors for organic field effect transistors (OFETs).[11,12] Several studies have highlighted the cooperative effect promoted by H-bonds[13] or conjugated covalent bonds[11,12,14–17] between DPP derivatives on their functional properties. Particularly, DPP-based conjugated polymers (CPs) are benchmark CPs for high-performance organic semiconductors.[7] However, *N*-alkylation, which can significantly increase the production costs, is required to prevent π–π stacking and ensure the solubility and processability of DPP-based CPs.[11,12,14–17] In addition, the synthesis of DPP-based CPs implies multistep processes catalysed by expensive and toxic derivatives (*e.g.* tin and palladium-based compounds).[11,12,15–17] Furthermore, purification of DPP-based CPs remain limited to column chromatography,[11,12,16] which further increases costs and constitutes an additional hurdle to scaling-up.

Oxidative chemical vapor deposition (oCVD), which relies on the vapor phase transport of aromatic compounds and their subsequent reaction with an oxidizing agent to readily form conjugated polymers directly in thin film form,[18] constitutes an attractive alternative to solution-based methods. oCVD possesses several assets, such as conformality, substrate independence and excellent control of the film parameters (thickness, porosity).[18,19] In recent years, oCVD has been successfully used in a broad range of research fields and applications, including photovoltaic,[20] catalysis,[21] energy storage,[22] and gas sensing.[23] Noteworthy, Gharahcheshmeh *et al.* used water-assisted oCVD to engineering the π–π stacking in poly(3,4-ethylenedioxy-thiophene) (PEDOT) thin films and reached a record-high electrical conductivity of 7520 S cm^{-1}.[24] Indeed, macromolecular conformation is well known to play a significant role on the properties of polymeric materials.[25–28] Particularly, reduced

[a] *Materials Research and Technology Department, Luxembourg Institute of Science and Technology, L-4362 Esch-sur-Alzette, Luxembourg.*
E-mail: nicolas.boscher@list.lu
[b] *Center for Soft Nanoscience, University of Münster, Münster 48149, Germany*
[c] *Physics Institute, University of Münster, Münster 48149, Germany*
[d] *Faculty of Chemistry, Warsaw University of Technology, 00-664 Warszawa, Poland*
[e] *Institute of Physical Chemistry, Polish Academy of Sciences, 01-224 Warszawa, Poland*
[f] *Faculty of Chemistry, University of Warsaw, 02-093 Warszawa, Poland*

intermolecular distances can yield superior charge carrier density and mobility, improved delocalization and electrical conductivities.[29–31] Being a solvent-free process, oCVD suppresses the need for solubilizing substituents that both hinder π–π stacking and prevent the integration of more advanced groups. Recently, Bengasi *et al.* implemented the oCVD strategy for the simultaneous synthesis and deposition of porphyrin-based CPs.[32] The decoupling of the porphyrin substituents from the synthesis requirement allowed the synthesis of porphyrin-based CPs bearing unexplored groups.[21,30] Particularly, the use of small substituents, *i.e.* phenyl, enabled to reduce intermolecular distances and improve π–π stacking,[23,30] yielding superior conductivities for porphyrin-based CPs.[30]

Taking advantage of the potential of oCVD, we investigate in this work the oCVD reaction of DPP derivatives with the aim to enable both the formation of conjugated covalent bonds and H-bonds in DPP-based CPs thin films. To this end, we selected both *N*-unsubstituted and *N*-alkylated DPP derivatives flanked with electron-rich thienyl moieties that provide active sites for oxidative polymerization. The occurrence of the oxidative coupling reaction was evidenced by ultraviolet-visible-near infrared (UV-Vis-NIR) spectroscopy and laser desorption ionization high-resolution mass spectrometry (LDI-HRMS). The influence of the *N*-substituent on the electronic properties of the DPP-based CPs thin films was evaluated using two-photon photoelectron spectroscopy (2PPE). 2PPE uses a first photon to excite an electron into an intermediate state and a second photon for probing. By varying the time delays between pump and probe pulse, 2PPE allows the exploration of excited states dynamics. In contrast to purely optical spectroscopy methods, optically dark states can be investigated directly. Further, the high surface sensitivity, inherent to the method, makes 2PPE suitable for thin film characterisation.[33] The data obtained give direct access to the fundamental processes of charge generation in organic semiconducting devices, *e.g.* exciton,[34–38] triplet[33,39–44] and polaron generation,[45–47] which are controlled by the macromolecular conformation. Indeed, vibronic and electronic coupling is influenced by the molecular structure, and π–π stacking can induce a photocurrent enhancement.[34,35,48–53]

Results and discussion

Gas phase synthesis of thiophene–diketopyrrolopyrrole conjugated polymer thin films

Our investigations towards the chemical vapor deposition of thienyl-bridged diketopyrrolopyrrole polymers began with the oCVD reaction of 3,6-di(2-thienyl)-2,5-dihydropyrrolo[3,4-*c*]-pyrrole-1,4-dione (TDPP) (Table S1, ESI†). Electron-rich thienyl groups are selected as core-substituents to provide active sites for the intermolecular oxidative polymerization. Among the commercially available thienyl core substituted DPP derivatives, TDPP constitutes the simplest motif, bearing no substituent at its axial positions (*N*-positions). Alkyl chains, which are commonly used as axial substituents to grant solubility to TDPP-based polymers (blocking H-bonding and reducing π–π
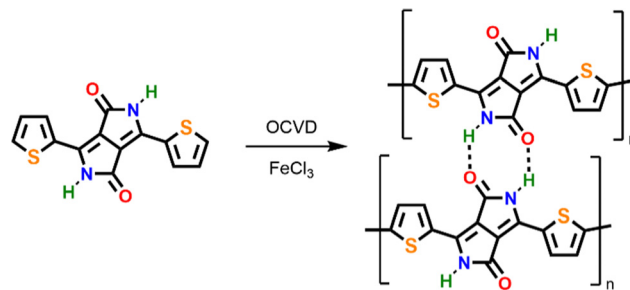
Scheme 1 Molecular structures of TDPP (left) and the conjugated polymer (right) formed from the oxidative intermolecular coupling reaction of TDPP through the α position of the thienyl substituent in the presence of FeCl₃. Due to the unsubstituted axial positions of TDPP, hydrogen bonds between TDPP monomers, oligomers and polymer chains are also possible and can yield strong intermolecular interactions. One should note here that intermolecular coupling may also occur through the normally less-reactive β position of thienyl substituent.

stacking),[11,12,14–17] are not required in oCVD since the synthesis, deposition and integration are performed simultaneously.[18,21,23,30,32] Iron(III) chloride (FeCl₃) was selected due to its ability to promote the dehydrogenative coupling of both thiophene compounds[54] and heterocyclic macrocycles.[21,23,30,32] Prior to its sublimation under oxidative conditions, the thermal stability of TDPP was controlled by thermogravimetry (Fig. S1, ESI†), which reveals a stability up to at least 300 °C. The oCVD reaction of TDPP and FeCl₃ (Scheme 1) was undertaken under reduced pressure (10^{-3} mbar) in a custom-built reactor equipped with two crucibles used to simultaneously sublime TDPP (255 °C) and FeCl₃ (170 °C) towards a heated stage (200 °C) on which were placed the substrates (Scheme S1, ESI†).

The oCVD reaction of TDPP with FeCl₃ leads to the formation of deep blue coatings (denoted **pTDPP**) that contrasts with the vivid pink color of the coatings obtained from the sublimation of TDPP (denoted **sTDPP**) (Fig. 1). Such a color change, from pink to blue, suggests the expansion of the chromophore and the formation of TDPP oligomers. Indeed, Casutt *et al.* previously described that TDPP dimers exhibit dark violet color,[3] whereas the parental Boc-substituted TDPP monomer exhibits a yellow-orange coloration. UV/Vis/NIR spectroscopy, performed on coated borosilicate glass substrates, confirms significant differences in the absorption spectrum of the deep blue **pTDPP** coating with respect to the vivid pink **sTDPP** coating. Particularly, upon reaction with FeCl₃, the absorption maximum undergoes a bathochromic shift from 564 nm in **sTDPP** to 650 nm in **pTDPP**. The bathochromic shift of the absorption maximum, assigned to the π–π* transition, suggests the enlargement of the conjugation length through an oxidative polymerization process. This band is observed at a slightly lower wavelength than previously reported ones for DPP copolymers that are often copolymerized with multiple donor units to enhance donor–acceptor interactions and further reduce band gap.[55–57] One can note here the bathochromic shift of the main absorption peaks (514 and 564 nm) of the **sTDPP** coating by comparison to the positions of the main absorption peaks of TDPP in solution (488 and 525 nm).[58] Importantly,
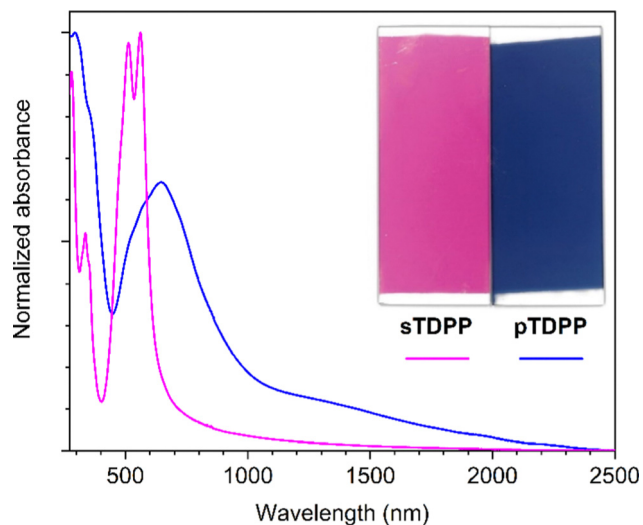
Fig. 1 Optical images (inset) and UV/Vis/NIR absorption spectra of the sublimed **sTDPP** coating (pink) and oCVD **pTDPP** coating (blue) prepared from TDPP on glass substrates.

pTDPP exhibits a broad absorption in the NIR region, up to 2400 nm (Fig. 1). Upon doping with $FeCl_3$, positive polarons or positive bipolarons form and induce the generation of localized electronic states, above and below the valence and conduction bands, respectively. Therefore the transitions related to these new localized electronic states yield absorption bands at higher wavelengths. Particularly, the NIR absorption band observed at high doping levels can be assigned to the transition related to bipolarons. According to the observations previously reported for hydrogen bonded TDPP dimers,[3] the **pTDPP** coating is insoluble in common organic solvents, including dimethyl sulfoxide (DMSO) (Fig. S2, ESI†). This contrasts with the **sTDPP** coating which is fully soluble in DMSO (Fig. S2 and S3, ESI†).

LDI-HRMS analysis directly performed on the **pTDPP** coating reveals the formation of TDPP oligomers confirming the successful intermolecular coupling of TDPP under oCVD conditions (Fig. 2). Up to tetrameric oligomers are observed in the mass spectrum of **pTDPP**, while only monomeric species are observed for **sTDPP**. One should note here that LDI-HRMS analysis, with an instrumental limit of 4000 m/z, does not provide an exhaustive view into the mass distribution. Therefore, formation of longer oligomers, with masses outside the instrumental limit, is conceivable. Moreover, the intensities related to the detected species are not directly related to their abundance. Unfortunately, the insolubility of the **pTDPP** coating (Fig. S2, ESI†) prohibits GPC analysis and a thorough characterization of the oCVD coating. In addition to the oxidative coupling of TDPP, LDI-HRMS evidences the integration of one to several chlorines (Fig. 2b), which could also contribute to the very weak solubility of **pTDPP**. Analysis of the Cl 1s XPS spectrum confirms the presence of an organic chloride environment related to the chlorination of the TDPP oligomeric and polymeric species (Fig. S4, ESI†). Chlorination is a well-known side reaction in oCVD processes that involve metal chlorides as oxidants.[59]

With the aim to perform a GPC analysis and undoubtedly demonstrate the oxidative polymerization of TDPP in oCVD, we investigated the oCVD reaction of 2,5-bis(2-ethylhexyl)-3,6-di(2-thienyl)-2,5-dihydropyrrolo[3,4-c]pyrrole-1,4-dione (BEHTDPP). In accordance with previous solution-based studies, the grafting of long alkyl chains to the axial positions of the TDPP motif is foreseen to confer solubility to the formed polymeric chains by reducing π–π intermolecular interactions between the aromatics systems, and by preventing hydrogen bonding between amide functional groups.[11,12,14–17] In addition to the 2-ethylhexyl group, we also investigated the oCVD reaction of TDPP substituted with one or two *tert*-butyloxycarbonyl (boc) protecting groups. However, the low-pressure (10^{-3} mbar) and
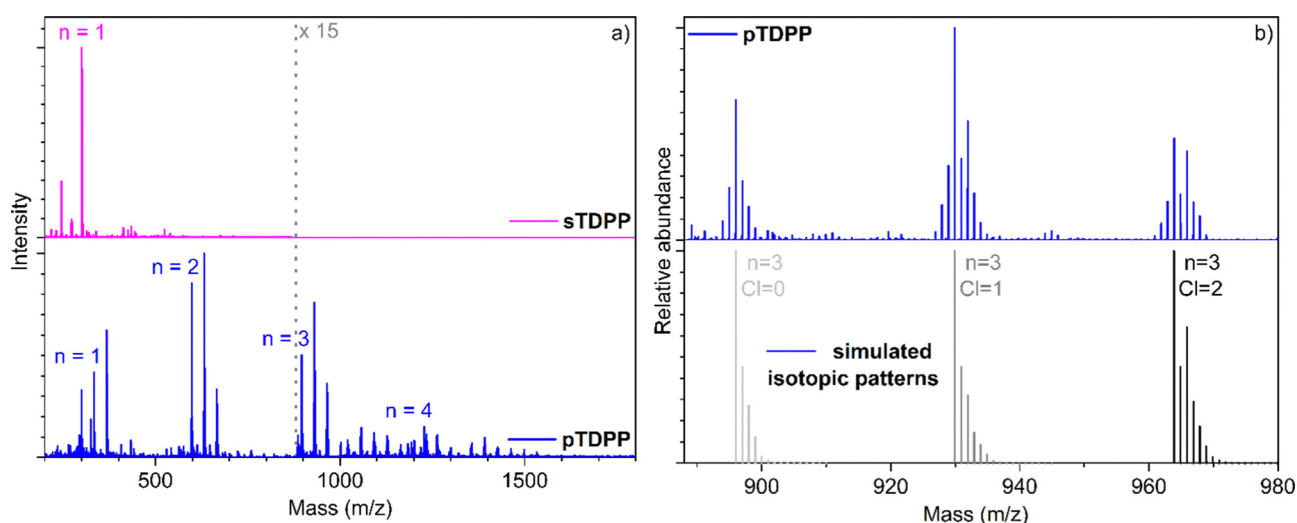

Fig. 2 (a) LDI-HRMS spectra of the sublimed **sTDPP** coating (pink) and oCVD **pTDPP** coating (blue) prepared from TDPP. (b) LDI-HRMS spectra of the trimeric region tha shows integration of chlorine atoms, a well-known side reaction in oCVD when using chlorinated oxidants. Experimental LDI-HRMS spectrum of **pTDPP** is displayed (blue) alongside simulated isotopic patterns of trimeric species bearing 0 ([(TDPP)$_3$−2H]$^+$, light grey), 1 ([(TDPP)$_3$−3H + 1Cl]$^+$, dark grey) and 2 chlorine atoms ([(TDPP)$_3$−4H + 2Cl]$^+$, black).

temperature (200 °C) operating conditions required to supply the TDPP-based monomers from the vapor phase in the proposed CVD approach yield to the removal of the Boc group during sublimation step (Fig. S1, ESI†).

Similarly to what is observed for TDPP, the oCVD reaction of BEHTDPP with $FeCl_3$ (Table S1 and Scheme S2, ESI†) yields the formation of coatings (denoted **pBEHTDPP**) whose color (brownish to greyish) contrasts with the color (pinkish) of the coatings prepared from the sole sublimation of BEHTDPP (denoted **sBEHTDPP**) (Fig. S5, ESI†). UV/Vis/NIR spectroscopy analysis confirmed significant differences in the absorption spectrum of **sBEHTDPP** and **pBEHTDPP** coating (Fig. S5, ESI†). Such as for TDPP, upon reaction with $FeCl_3$, the absorption maximum undergoes a bathochromic shift from 506 nm in **sBEHTDPP** to 658 nm in **pBEHTDPP**. Although less pronounced than for **pTDPP** (Fig. 1), **pBEHTDPP** also exhibits absorption in the NIR region, up to 2200 nm (Fig. S5, ESI†). LDI-HRMS analysis directly performed on the **pBEHTDPP** coating reveals the formation of BEHTDPP oligomers, confirming the successful intermolecular coupling of BEHTDPP (Fig. 3a). Up to trimeric species are observed in the mass spectrum of **pBEHTDPP**, while only monomeric species are observed for **sBEHTDPP**. The GPC analysis of **pBEHTDPP** (Fig. 3b) confirms the formation of polymeric chains under oCVD condition. Satisfactorily, monomer and short oligomers are not detected by GPC which only displays a broad peak pointing to masses up to 32 000 g mol^{-1}. Given the similarities in the UV/Vis/NIR (Fig. 1 & Fig. S5, ESI†) and LDI-HRMS spectra (Fig. 2 and 3a) of **pTDPP** and **pBEHTDPP**, one may assume that the **pTDPP** samples are also composed of polymer chains with molecular weights in the range of tens of thousands g mol^{-1}.

Scanning electron microscopy (SEM) and atomic force microscopy (AFM) of **sTDPP** and **pTDPP** reveal the formation of rather dense coatings with a rugged surface (Fig. 4). Upon polymerization, the size of the main features observed at the

surface increase from 50 to 100 nm, respectively. Contrarily, **sBEHTDPP** and **pBEHTDPP** exhibit far less features at their surface (Fig. S6 and S7, ESI†), which strongly contrast with the morphology of the coatings grown from TDPP. Indeed, the long alkyl chains attached to the axial positions of the TDPP motif in BEHTDPP reduce the π–π interactions. Beyond enabling a higher solubility, reduction of π–π stacking is also responsible for the lower sticking coefficient of the BEHTDPP monomeric units, yielding a lower sublimation temperature despite of a higher molecular weight (155 °C for BEHTDPP against 255 °C for TDPP) and a higher mobility at the surface of the substrate. Thus, in addition of influencing the packing arrangement of the DPP-based compounds,[60] alkyl axial substituents can affect their mobility and supramolecular aggregation. Interestingly in the perspective of optoelectronic applications, **pTDPP** exhibit a low surface roughness with an arithmetic mean height (Sa), *i.e.* mean difference in height from the mean plane, close to 2 nm.

Electronic properties of the thiophene–diketopyrrolopyrrole conjugated polymer thin films

Fostered by the straightforward synthetic and deposition approach reported above, the following section is exploring the electronic and electrochemical behavior of thin films of unsubstituted thiophene–diketopyrrolopyrrole conjugated polymer (**pTDPP**). The current–voltage ($I(V)$) characteristics of **sTDPP** and **pTDPP** deposited onto chips patterned with interdigitated electrodes revealed an ohmic behaviour (Fig. 5a). As expected, the dehydrogenative coupling of the TDPP units, which yield the formation of a conjugated backbone, induces a strong increase of the electrical conductivity from 7.8×10^{-10} S cm^{-1} for **sTDPP** to 1.7×10^{-3} S cm^{-1} in **pTDPP**. Noteworthy, the oCVD **pBEHTDPP** coating exhibits a reduced conductivity (9.7×10^{-5} S cm^{-1}) compared to **pTDPP** (Fig. 5b and Fig. S8, ESI†). The discrepancy between the conductivities of **pTDPP** and **pBEHTDPP** coatings
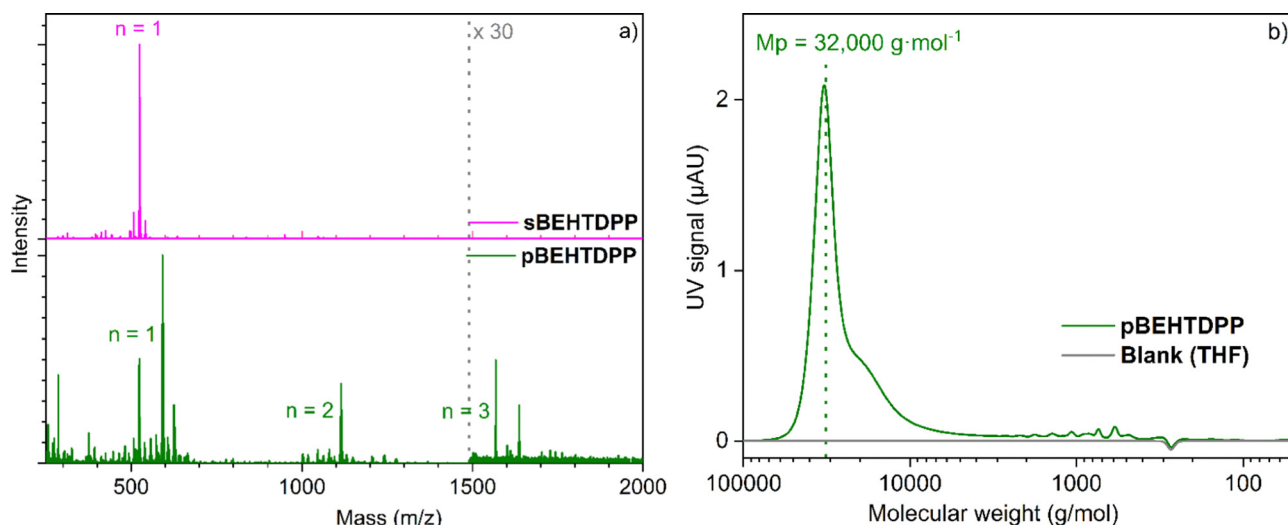

Fig. 3 (a) LDI-HRMS spectra of the sublimed **sBEHTDPP** coating (pink) and (b) oCVD **pBEHTDPP** coating (grey) prepared from TDPP and (b) GPC spectrum of **pBEDTDPP**.
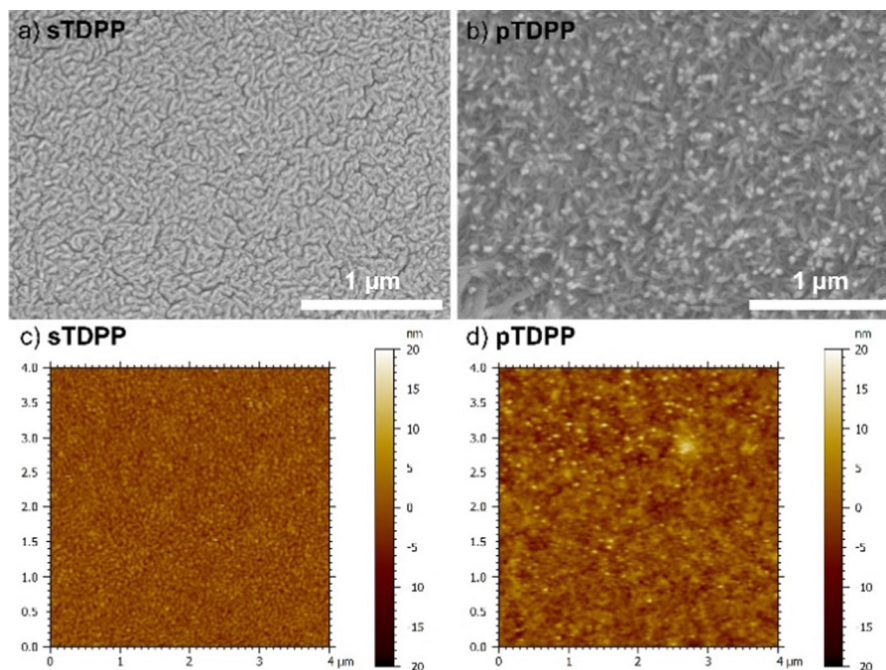
Fig. 4 (a and b) High magnification SEM images and (c and d) AFM topography images of the sublimed **sTDPP** coating (a and c) and oCVD **pTDPP** coating (b and d) prepared from TDPP.
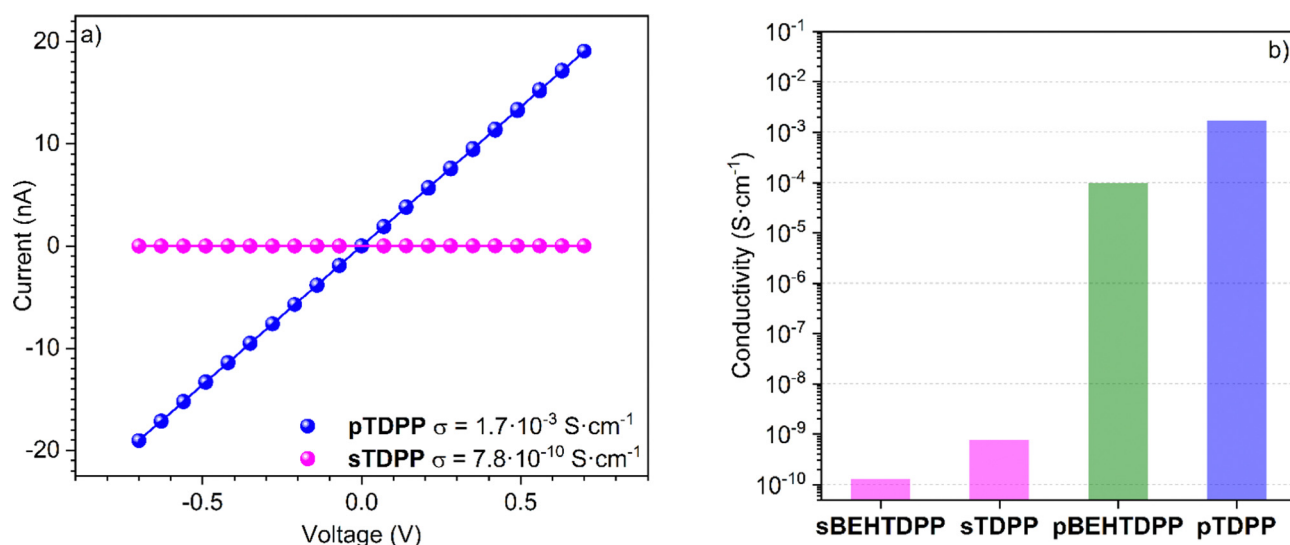

Fig. 5 (a) Lateral electrical conductivity measurement of sublimed **sTDPP** coating (pink dots) and oCVD **pTDPP** coating (blue dots) on interdigitated chips. Pink and blue solid lines show the linear fits used to determine the conductivities. (b) Histogram of electrical conductivity values for the sublimed and oCVD coatings.

likely arises from a reduced intermolecular π–π stacking in the presence of long axial alkyl substituents. Limited intermolecular π–π stacking due to bulky substituents is a strong limitation into the photovoltaic or electronic performances of conjugated polymers.[61] Thus, the ability to readily polymerize and deposit diketopyrrolopyrrole-based polymer irrespective of their substituents should rapidly improve the properties of these materials.

Such as for other conjugated polymers, the repetition of σ and π bonds along the oligomeric and polymeric chains

constituting **pTDPP** is expected to give rise to a delocalization of π orbitals and of an energy level splitting of the π bonds. Analysis of the valence band region of the XPS spectra allows to estimate the valence band (VB) or highest occupied molecular orbital (HOMO) position of the **sTDPP** and **pTDPP**. In particular, the valence band maximum (VBM), determined from the extrapolation of the linear fit of the leading edges of the spectra to the baseline, is shifted from 1.53 eV (**sTDPP**) to 0.99 eV (**pTDPP**) upon oxidative polymerisation (Fig. S9, ESI†).
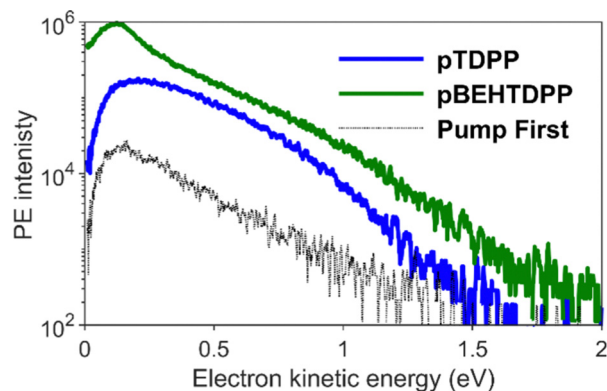
Fig. 6 Photoelectron spectra of **pTDPP** (blue) and **pBEHTDPP** (green) measured with an excitation of $h\nu_{pump}$ = 1.88 eV and $h\nu_{probe}$ = 4.8 eV at a delay of $\Delta\tau$ = 300 fs, where the 2PPE signal strength reaches its maximum. For comparison, a spectrum of **pTDPP** is shown in black where the sample pulse arrives at the sample before the probe pulse.

This observation is consistent with the expansion of π-electronic system known to raise the energy of the HOMO.

From the photoelectron spectra of the maximum 2PPE signals shown in Fig. 6, one can observe a clean broad spectrum with photoelectrons up to E_{kin} = 1.5 eV for **pTDPP**, and the typical increasing intensity towards lower kinetic energy, usually caused by secondary electrons. Comparing the spectrum of **pTDPP** with highest 2PPE intensity, which occurs at a pump – probe delay of $\Delta\tau$ = 300 fs, with the background spectrum (pump pulse first), a clear 2PPE feature is identified, centred around E_{kin} = 0.4–0.8 eV. The spectrum for **pBEHTDPP** shows a very similar pattern, but somewhat higher in intensity and with a more pronounced peak from secondary electrons at lower kinetic energies.

The time-resolved dynamics were analysed as a multi-exponential decay and can be described adequately by four distinguishable individual lifetimes. It is worth noting that a fourfold exponential decay model, in its simplicity, represents the most straightforward approach. However, we want to mention commonly employed alternative methods which consider that a rapidly decaying state feeds a longer living state. In this cascaded model, a longer living state therefore has initially zero intensity and rises with a time constant which reflects the lifetime of the rapid decay.[62] From a physical point of view, the overall excited state dynamics in conjugated polymers can accurately be depicted by a set of rate equations featuring interconnected states.[63–66] Following extensive testing, a cascaded model and approaches with fitted rate equations resulted not in substantially improved or different lifetimes and their relative intensities. Further, there is no clear indication of rising components in the tr-2PPE data, see also the two-dimensional presentation in Fig. S10 (ESI†). Thus, we conclude that our more phenomenological description is entirely adequate.

For both **pTDPP** and **pBEHTDPP**, an ultrafast lifetime in the femtosecond scale ($\tau_1 \sim$ 100 fs), two intermediates with a few picoseconds $\tau_2 \sim$ 1 ps, $\tau_3 \sim$ 5 ps, and a very long lifetime $\tau_4 \gg$ 50 ps, beyond our measurement range, are obtained.

These lifetimes τ_k and also their amplitudes A_k are of similar orders of magnitude for both samples, but depend on the electron kinetic energy. Fig. 7a shows the fitted decay times τ_1, τ_2, τ_3 for **pTDPP** (blue data) and **pBEHTDPP** (green data) in the range of low kinetic energies from E_{kin} = 0.2 eV up to higher kinetic energies of E_{kin} = 1.0 eV, each integrated over a width of ΔE_{kin} = 100 meV. The general trend shows a slight increase for all three independent lifetimes towards lower kinetic energies. The lifetimes for **pTDPP** are consistently longer than those of **pBEHDPP**. Moreover, the difference is larger for lower kinetic energies, which is particularly evident in the ultrafast lifetime τ_1. For **pBEHDPP** the short lifetime, $\tau_1 \sim$ 60 fs, is on the order of the pump and probe pulse cross-correlation and probably limited by this. For **pTDPP**, the short lifetime of $\tau_1 \sim$ 120 fs is nearly twice as long. This difference in the accumulation of the charge carrier generation can also be seen clearly in the inset of Fig. 7c.

The temporal evolution of the 2PPE signal for high (Fig. 7b) and for low kinetic energies (Fig. 7c) was recorded and fitted. The decay curves for high kinetic energies are almost identical for the polymer with (**pBEHTDPP**) and without (**pTDPP**) N-substituents (Fig. 7b). It can be described almost completely by a double exponential decay ($A_4 \sim$ 0% and $A_3 \sim$ 0%, Fig. S11, ESI†). In contrast, at low energies (Fig. 7c) a long living component manifests itself in an offset in the data for **pTDPP** compared to the polymer with N-alkyl substituents (**pBEHTDPP**) at lifetimes $\Delta\tau >$ 10 ps. The decay of this long living component cannot accurately be measured by our delay stage and is therefore set as constant to infinity. However, the difference in the offset is clearly visible in the development of its amplitude A_4 in Fig. 7d.

This long living component, accounted by A_4, typically reflects a variety of charge generating quasiparticles. Evidence is mounting that free charge carriers can be generated quasi instantaneously in conjugated polymers upon excitation. Moreover, the correct arrangement of TDPP molecules can enable singlet fission, which, in particular, is a promising mechanism for increasing the efficiency of organic solar cell components.[63,64,67–69] For TDPP and derivates, up to 200% triplet exciton quantum efficiency have been measured,[64] interestingly, in connection with a higher yield for entities with shorter side chains. Singlet fission occurs within tens of picoseconds and can be stabilised by expanded π-skeletons of the molecules.[70] Polarons and triplet excitons typically have lifetimes in the nano- to microsecond range.[39,43,67,71] Even though it is not possible to distinguish both directly, the offset at long lifetimes is indicative for an increased charge carrier generation. Another indication is the course of the relative amplitudes with varying electron energy. Whereas the high-energy range can be described biexponentially, it is evident that for lower kinetic energies the relative contributions of the fast lifetimes decrease and the contributions of the slower ones increase, in particular for **pTDPP**. The lower kinetic energies represent states between the VBM and the LUMO, typically charge transfer excitons, polarons and triplets. Under the assumption of a binding energy of E_B^{LUMO} = −3.9 eV and a
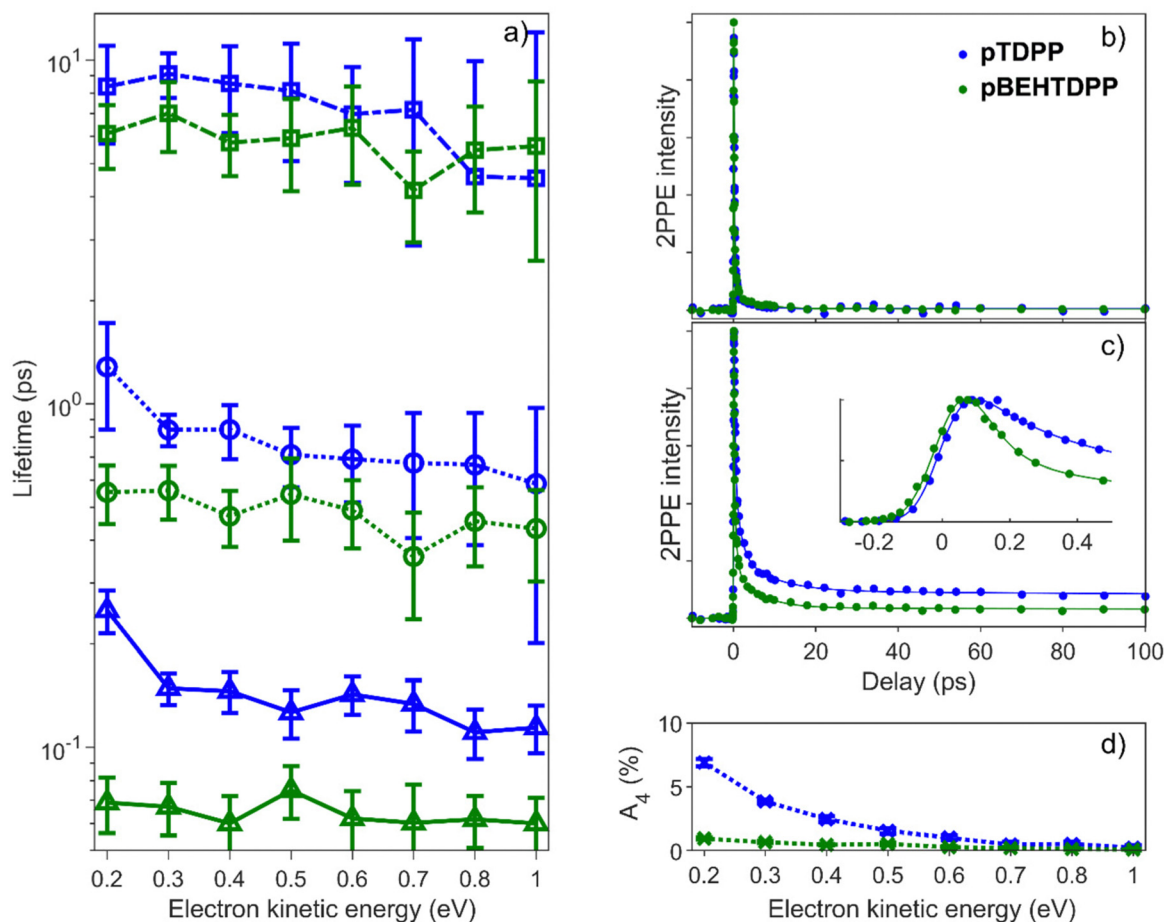
Fig. 7 Time resolved evolution of the 2PPE signal measured on **pTDPP** (blue) and **pBEHTDPP** (green) with an excitation of hv_{pump} = 1.88 eV and hv_{probe} = 4.8 eV, (a) show the trend of the three fitted lifetimes as a function of the kinetic energy in the 2PPE spectrum, (b) decay for E_{kin} = 1 eV, (c) decay for E_{kin} = 0.2 eV. Solid lines correspond to the respective multi-exponential fit, the inset shows a zoom around the temporal overlap. Panel (d) depicts the contribution of the longest lifetime to the signal as a function of kinetic electron energy.

photon energy of the probe pulse of hv_{probe} = 4.8 eV, the LUMO is represented in the 2PPE spectra at a kinetic energy of E_{kin} = 0.9 eV.

The temporal evolution at energies around and above the LUMO shows for both samples a much faster decay than at lower energies. In particular, the ultrafast decays τ_1 and τ_2 are present with $A_1 \sim$ 90% and $A_2 \sim$ 10% (Fig. S11, ESI†). The decay in the range of $\tau_1 \sim$ 100 fs is predominantly associated with the excitation of higher vibronic states.[41,72] Exciton self-trapping, polaron (pair) formation,[45,47,65,73,74] and local relaxations are also expected on this time scale, although the former is probably even below our temporal resolution (<30 fs).[36,40,45] The decay times of the LUMO then results in τ_2 = (0.6 ± 0.4) ps and τ_2 = (0.5 ± 0.1) ps for **pTDPP** and **pBEHTDPP**, respectively, and are therefore not significantly different. Fig. 7a shows, however, that for both τ_1 and τ_2, the lifetimes for **pTDPP** are systematically longer over the entire kinetic energy range than those of **pBEHTDPP**. We ascribe this phenomenon to the absence and presence, respectively, of the side chains. The additional alkyl groups in **pBEHTDPP** probably cause a broader spatial distribution of the excited state over the backbone, and therefore opens additional pathways to undergo a fast

relaxation. On one hand, this leads to an increased lifetime in **pTDPP** of the initial excitation, while on the other hand, its relative contribution A_1 is decreased (Fig. S11, ESI†).

For the comparison of the medium-long lifetime τ_3, the same systematic behaviour is observed. For **pTDPP** and at lower kinetic energies, this lifetime is slightly longer, than that of **pBEHTDPP**. The relative proportion of this decay component also increases towards lower kinetic energies. Whereas this relative amount remains rather small for **pBEHTDPP** (increases from A_3 = 1% to a maximum of 4%) it grows to 12% for **pTDPP**. Lifetimes of approx. 5–12 ps are typical for hot intramolecular charge transfer processes,[36,45] and facilitate free charge generation.[45,74,75] In addition, this lifetime is of the order of that for generation of the $^1(T_1T_1)$- state measured for several thin films of TDPP monomers. This generation time was measured to be a few tens of picoseconds for different kinds of side chains.[64,67] Roy and Dasgupta measured the formation of a triplet pair from the first excited state within about 700 fs in TDPP nanoparticles, remarkably close to the lifetime τ_2 for both polymers in the present measurement.[36] The energy of the monomer TDPP triplet is about 1.1 eV above the VBM and

appears around $E_{kin} = 0.2$ eV in the 2PPE spectra, the energy region where the contributions of A_3 and A_4 are also increasing.[43,49,64] Shivhare *et al.* measured a negligible offset in the picosecond time scale for thiophene/DPP polymers, but an enhanced offset in combination with PCBM, and attributed this to the charge concentration.[66] The longevity of charge signatures facilitated through enhanced hydrogen bonds is in accord with the results by Ávila-Rovelo *et al.* in thiophene-capped DPP molecules.[52]

The ability to synthesize *N*-unsubstituted thiophene–diketopyrrolopyrrole conjugated polymers and readily deposit them in the form smooth, dense and thickness-controlled thin films constitutes a breakthrough in the field of DPP-based conjugated polymers. Particularly, the simplicity of the proposed CVD method contrasts with recently developed solution-based approach towards the synthesis of DPP-based blue-colored pigments, which involves (i) tetrahydrofuran, chloroform, and toluene as solvents, (ii) di-*tert*-butyl decarbonate, *N*-bromosuccinimide and tetrakis(triphenylphosphine) palladium for grafting boc groups and enabling the Stille coupling, and (iii) a thermal treatment (190 °C) in the presence trifluoromethylsulfonic acid to ensure a complete removal of the boc group.[3] Thus, the oCVD reaction of DPP derivatives should allow to go far beyond the state-of-the-art of DPP-based materials by eliminating the restrictions dictated by solution-based approaches and allowing the synthesis, engineering and integration of DPP-based conjugated polymers for optoelectronic and catalytic applications. Further improvements may also involve the use of liquid oxidants, such as antimony pentachloride ($SbCl_5$) and vanadium oxytrichloride ($VOCl_3$),[76–78] in replacement of solid oxidants like $FeCl_3$ or $CuCl_2$ whose by-products remain in the oCVD coatings.[59] Moreover, the delivery rate of liquid oxidants can be more precisely regulated, resulting in better control of the oxidant to monomer ratio.

Conclusions

In summary, the proposed CVD method provides a straightforward solventless and scalable approach for the facile synthesis, engineering and integration of DPP-based conjugated polymers for thin films applications. In this first demonstration, and in contrast to solution-based strategies, the oxidative polymerization and H-bonding of an *N*-unsubstituted DPP derivative was successfully achieved. Noteworthy, the new conjugated TDPP polymer was readily deposited as uniform and low-roughness thin films on various substrates. Interestingly, the DPP-based conjugated polymer (**pTDPP**) without *N*-alkyl substituent exhibits a higher conductivity and a slight but systematic increase of all lifetimes, notably an increase in the fraction of the very long-lived excited species associated with the free charge carriers or their precursors.

Experimental

Oxidative chemical vapor deposition

The oCVD experiments were performed in a custom-built oCVD reactor equipped with two evaporators (Scheme S1, ESI†).

Evaporators were loaded with 3,6-di(2-thienyl)-2,5-dihydropyrrolo-[3,4-*c*]pyrrole-1,4-dione (TDPP) or 2,5-bis(2-ethylhexyl)-3,6-di(2-thienyl)-2,5-dihydropyrrolo[3,4-*c*]pyrrole-1,4-dione (BEHTDPP) and iron (III) chloride ($FeCl_3$) and heated to 255 °C, 155 °C and 170 °C, respectively (Table S1, ESI†). $FeCl_3$ was obtained from Sigma-Aldrich (97%) and TDPP[79] and BEHTDPP[80] were synthesized according to literature. The chamber was fed with argon and maintained to a pressure of 10^{-3} mbar. Deposition time was set to 30 min for all experiments. Microscope borosilicate glass slides (Menzel-Gläser), silicon wafers (Siltronix), FTO-coated glass and chips patterned with interdigitated gold electrodes (Fraunhofer IPMS) were employed.

Thin film characterization

The thickness of the films was measured by using an Alpha Step D-500 profilometer from KLAvTencor. Optical absorbance was measured in the range 250–2500 nm using an UV/Vis/NIR spectrophotometer with a 150 mm diameter integrating sphere (PerkinElmer, Lambda 950). Atmospheric-pressure laser desorption/ionization high-resolution mass spectrometry (AP-LDI-HRMS) was performed directly on the as-deposited films without any matrix deposition using a LTQ/Orbitrap Elite Hybrid Linear Ion Trap-Orbitrap mass spectrometer from Thermo Scientific coupled AP-MALDI (ng) UHR source from MassTech Inc. equipped with a 355 nm Nd:YAG laser. An in-source decay (ISD) of 70 V was applied to the films to prevent the detection of non-covalent TDPP or BEHTDPP clusters that could interfere with the detection of the desorbed oligomers. A maximum injection time of 800 ms and a resolving power of 240 000 at m/z 400 within the normal mass range (m/z 300–1000) and the high mass range (m/z 1000–4000) were employed for the HRMS analyses.

The electrical conductivity was evaluated from the films deposited on chips patterned with interdigitated gold electrodes and stored in the laboratory under ambient conditions. The current–voltage scans were recorded using a two-point probe and conductivity was evaluated using the Ohm's law. Cyclic voltammograms of the films deposited on FTO-coated glass were registered using an Autolab potentiostat, which was also used for the spectroelectrochemical studies. In order to determine the background current, the CV curves were registered for bare FTO-coated glass. The currents recorded for the polymer films were at least two orders of magnitude larger than that observed for uncovered FTO glass substrates.

The UV/Vis/NIR spectra were recorded using Cary 5000 spectrophotometer. After cleaning and rinsing with dichloromethane and drying, the films deposited on FTO-coated glass were placed under an argon atmosphere in a measuring cell equipped with Ag/Ag^+ reference electrode and filled with 0.1 M Bu_4NPF_6/acetonitrile electrolyte. The spectroelectrochemical measurements were performed in quasi-static mode during which the working electrode was polarized in small steps. After each potential change, a wait time was applied until the measured current dropped to zero or to negligible value.

UPS spectra were measured with a hemispherical analyser (Specs Phoibos 150) and a cold cathode capillary discharge

Helium lamp (He-I, $h\nu$ = 21.22 eV). The valence band maximum is given against the Fermi energy of the system. The sample was placed in vacuum with a base pressure of 2×10^{-10} mbar.

A fibre laser (Active Fiber Systems, λ = 1030 nm, repetition rate f_{rep} = 500 kHz, $\tau_{FWHM} < 40$ fs pulse duration) is split into two separate output beams. One beam is converted to the 4th harmonic (s-polarized, λ = 257 nm, $h\nu$ = 4.8 eV, τ_{FWHM} = 65 ± 5 fs) by two optically nonlinear BBO crystals and utilized as the probe pulse. The other beam seeds a non-collinear optical parametric amplifier (NOPA) which generates pulses of about τ = 30 fs duration in the near infrared (Light Conversion, Orpheus N, tuneable λ = 650–950 nm, $h\nu$ = 1.9–1.3 eV, p-polarized). The frequency-converted pulses pass through two prism compressors to compensate for the dispersion of the optical paths. Before the pulses are spatially and temporally superimposed using a dielectric mirror, the infrared beam passes through a high-precision delay stage with a resolution of $\Delta\tau < 1$ fs (Physik Instrumente, PI M-405.DG). The sample is placed in an ultra-high vacuum chamber, and the kinetic energy of the emitted photoelectrons is analysed using a time-of-flight tube (eTOF) equipped with a delay line detector (Surface Concept, DLD 6565-4Q). A fourfold exponential function (1) was convoluted with a Gaussian corresponding to the width of the correlation of pump and probe pulse, τ_{cx} = 70 ± 5 fs, and was fitted to the time-resolved 2PPE signal. Here, τ_4 was fixed to infinity, as the lifetime $\Delta\tau \gg 50$ ps exceeds the range of the delay stage.

$$I_{2PPE} \sim \sum_k A_k \exp\left(\frac{\Delta\tau - \tau_0}{\tau_k}\right)\left(1 + \mathrm{erf}\left(\frac{\Delta\tau - \tau_0 - \tau_p^2/\tau_k}{\tau_p\sqrt{2}}\right)\right)$$ (1)

Author contributions

M. K. C.: conceptualization, synthesis, investigation, formal analysis, writing – original draft; T. K.: investigation, formal analysis, writing – original draft; K. K.: investigation, formal analysis, writing – review and editing; M. G.: synthesis, writing – review and editing; H. Z.: writing – review and editing; N. D. B.: conceptualization, methodology, investigation, formal analysis, funding acquisition, writing – original draft, writing – review and editing.

Conflicts of interest

There are no conflicts to declare.

Acknowledgements

References

1 D. G. Farnum, G. Mehta, G. G. I. Moore and F. P. Siegal, *Tetrahedron Lett.*, 1974, **15**, 2549–2552.
2 O. Zeman, V. Pelikan and J. Pachman, *ACS Sustainable Chem. Eng.*, 2022, **10**, 4788–4791.
3 M. Casutt, B. Dittmar, H. Makowska, T. Marszalek, S. Kushida, U. H. F. Bunz, J. Freudenberg, D. Jänsch and K. Müllen, *Chem. – Eur. J.*, 2019, **25**, 2723–2728.
4 A. Iqbal, M. Jost, R. Kirchmayr, J. Pfenninger, A. Rochat and O. Wallquist, *Bull. Soc. Chim. Belg.*, 1988, **97**, 615–644.
5 S. A. L. Shaikh, S. S. Birajdar, S. D. Ambore, A. L. Puyad, P. Vijayanand, S. V. Bhosale and S. V. Bhosale, *Results Chem.*, 2022, **4**, 100473.
6 M. Grzybowski and D. T. Gryko, *Adv. Opt. Mater.*, 2015, **3**, 280–320.
7 Q. Liu, S. E. Bottle and P. Sonar, *Adv. Mater.*, 2020, **32**, 1903882.
8 X. Song, N. Gasparini, M. M. Nahid, S. H. K. Paleti, C. Li, W. Li, H. Ade and D. Baran, *Adv. Funct. Mater.*, 2019, **29**, 1902441.
9 K. P. Sokol, W. E. Robinson, J. Warnan, N. Kornienko, M. M. Nowaczyk, A. Ruff, J. Z. Zhang and E. Reisner, *Nat. Energy*, 2018, **3**, 944–951.
10 L. Shen, Z. Tang, X. Wang, H. Liu, Y. Chen and X. Li, *Phys. Chem. Chem. Phys.*, 2018, **20**, 22997–23006.
11 B. Lim, H. Sun, J. Lee and Y.-Y. Noh, *Sci. Rep.*, 2017, **7**, 164.
12 K. Guo, J. Bai, Y. Jiang, Z. Wang, Y. Sui, Y. Deng, Y. Han, H. Tian and Y. Geng, *Adv. Funct. Mater.*, 2018, **28**, 1801097.
13 E. D. Głowacki, H. Coskun, M. A. Blood-Forsythe, U. Monkowius, L. Leonat, M. Grzybowski, D. Gryko, M. S. White, A. Aspuru-Guzik and N. S. Sariciftci, *Org. Electron.*, 2014, **15**, 3521–3528.
14 T. Reiker, Z. Liu, C. Winter, N. F. Kleimeier, D. Zhang and H. Zacharias, *J. Phys. Chem. C*, 2021, **125**, 5572–5580.
15 W. Li, K. H. Hendriks, M. M. Wienk and R. A. J. Janssen, *Acc. Chem. Res.*, 2016, **49**, 78–85.
16 R. Diao, H. Ye, Z. Yang, S. Zhang, K. Kong and J. Hua, *Polym. Chem.*, 2019, **10**, 6473–6480.
17 M. Li, J. Li, D. Di Carlo Rasi, F. J. M. Colberts, J. Wang, G. H. L. Heintges, B. Lin, W. Li, W. Ma, M. M. Wienk and R. A. J. Janssen, *Adv. Energy Mater.*, 2018, **8**, 1800550.
18 M. Heydari Gharahcheshmeh and K. K. Gleason, *Adv. Mater. Interfaces*, 2019, **6**, 1801564.
19 K. Baba, G. Bengasi, F. Loyer, J. P. C. Fernandes, D. El Assad, O. De Castro and N. D. Boscher, *ACS Appl. Mater. Interfaces*, 2020, **12**, 37732–37740.
20 R. M. Howden, E. J. Flores, V. Bulović and K. K. Gleason, *Org. Electron.*, 2013, **14**, 2257–2268.
21 D. Bansal, D. Cardenas-Morcoso and N. D. Boscher, *J. Mater. Chem. A*, 2023, **11**, 5188–5198.

22 P. Moni, J. Lau, A. C. Mohr, T. C. Lin, S. H. Tolbert, B. Dunn and K. K. Gleason, *ACS Appl. Energy Mater.*, 2018, **1**, 7093–7105.

23 G. Bengasi, R. Meunier-Prest, K. Baba, A. Kumar, A. L. Pellegrino, N. D. Boscher and M. Bouvet, *Adv. Electron. Mater.*, 2020, **6**, 2000812.

24 M. Heydari Gharahcheshmeh, M. T. Robinson, E. F. Gleason and K. K. Gleason, *Adv. Funct. Mater.*, 2021, **31**, 2008712.

25 B. J. Schwartz, *Annu. Rev. Phys. Chem.*, 2003, **54**, 141–172.

26 S. Chaudhry, Y. Wu, Z. Cao, S. Li, J. L. Canada, X. Gu, C. Risko and J. Mei, *Macromolecules*, 2021, **54**, 8207–8219.

27 K. Gu and Y.-L. Loo, *J. Polym. Sci., Part B: Polym. Phys.*, 2019, **57**, 1559–1571.

28 H. Li, M. E. DeCoster, C. Ming, M. Wang, Y. Chen, P. E. Hopkins, L. Chen and H. E. Katz, *Macromolecules*, 2019, **52**, 9804–9812.

29 X. Wang, X. Zhang, L. Sun, D. Lee, S. Lee, M. Wang, J. Zhao, Y. Shao-Horn, M. Dincă, T. Palacios and K. K. Gleason, *Sci. Adv.*, 2018, **4**, eaat5780.

30 G. Bengasi, J. S. Desport, K. Baba, J. P. Cosas Fernandes, O. De Castro, K. Heinze and N. D. Boscher, *RSC Adv.*, 2020, **10**, 7048–7057.

31 J. F. J. Ponder, S. A. Gregory, A. Atassi, A. K. Menon, A. W. Lang, L. R. Savagian, J. R. Reynolds and S. K. Yee, *J. Am. Chem. Soc.*, 2022, **144**, 1351–1360.

32 G. Bengasi, K. Baba, G. Frache, J. Desport, P. Gratia, K. Heinze and N. D. Boscher, *Angew. Chem., Int. Ed.*, 2019, **58**, 2103–2108.

33 G. D. Hale, S. J. Oldenburg and N. J. Halas, *Phys. Rev. B: Condens. Matter Mater. Phys.*, 1997, **55**, R16069.

34 X.-H. Jin, M. B. Price, J. R. Finnegan, C. E. Boott, J. M. Richter, A. Rao, S. M. Menke, R. H. Friend, G. R. Whittell and I. Manners, *Science*, 2018, **360**, 897–900.

35 A. De Sio, X. T. Nguyen and C. Lienau, *Z. Naturforsch., A: Phys. Sci.*, 2019, **74**, 721–737.

36 P. Roy and J. Dasgupta, *Pure Appl. Chem.*, 2020, **92**, 707–716.

37 E. Varene and P. Tegeder, *Appl. Phys. A: Mater. Sci. Process.*, 2012, **107**, 13–16.

38 L. Bogner, Z. Yang, S. Baum, M. Corso, R. Fitzner, P. Bäuerle, K. J. Franke, J. I. Pascual and P. Tegeder, *J. Phys. Chem. C*, 2016, **120**, 27268–27275.

39 J. R. Ochsmann, D. Chandran, D. W. Gehrig, H. Anwar, P. K. Madathil, K.-S. Lee and F. Laquai, *Macromol. Rapid Commun.*, 2015, **36**, 1122–1128.

40 A. E. Jailaubekov, A. P. Willard, J. R. Tritsch, W.-L. Chan, N. Sai, R. Gearba, L. G. Kaake, K. J. Williams, K. Leung, P. J. Rossky and X.-Y. Zhu, *Nat. Mater.*, 2013, **12**, 66–73.

41 A. A. Paraecattil and N. Banerji, *J. Am. Chem. Soc.*, 2014, **136**, 1472–1482.

42 T. A. Ford, I. Avilov, D. Beljonne and N. C. Greenham, *Phys. Rev. B: Condens. Matter Mater. Phys.*, 2005, **71**, 125212.

43 B. P. Karsten, R. K. M. Bouwer, J. C. Hummelen, R. M. Williams and R. A. J. Janssen, *Photochem. Photobiol. Sci.*, 2010, **9**, 1055–1065.

44 S. Vempati, L. Bogner, C. Richter, J.-C. Deinert, L. Foglia, L. Gierster and J. Stähler, *J. Chem. Phys.*, 2020, **152**, 74715.

45 P. Roy, A. Jha, V. B. Yasarapudi, T. Ram, B. Puttaraju, S. Patil and J. Dasgupta, *Nat. Commun.*, 2017, **8**, 1716.

46 E. L. Frankevich, A. A. Lymarev, I. Sokolik, F. E. Karasz, S. Blumstengel, R. H. Baughman and H. H. Hörhold, *Phys. Rev. B: Condens. Matter Mater. Phys.*, 1992, **46**, 9320–9324.

47 P. B. Miranda, D. Moses and A. J. Heeger, *Phys. Rev. B: Condens. Matter Mater. Phys.*, 2001, **64**, 81201.

48 I. Meager, R. S. Ashraf, S. Mollinger, B. C. Schroeder, H. Bronstein, D. Beatrup, M. S. Vezie, T. Kirchartz, A. Salleo, J. Nelson and I. McCulloch, *J. Am. Chem. Soc.*, 2013, **135**, 11537–11540.

49 M. Kirkus, L. Wang, S. Mothy, D. Beljonne, J. Cornil, R. A. J. Janssen and S. C. J. Meskers, *J. Phys. Chem. A*, 2012, **116**, 7927–7936.

50 O. G. Reid, J. A. N. Malik, G. Latini, S. Dayal, N. Kopidakis, C. Silva, N. Stingelin and G. Rumbles, *J. Polym. Sci., Part B: Polym. Phys.*, 2012, **50**, 27–37.

51 R. Meng and R. Zhu, *Sci. Rep.*, 2022, **12**, 10087.

52 N. R. Ávila-Rovelo, G. Martinez, W. Matsuda, S. Sinn, P. Lévêque, D. Schwaller, P. Mésini, S. Seki and A. Ruiz-Carretero, *J. Phys. Chem. C*, 2022, **126**, 10932–10939.

53 R. H. Friend, D. D. C. Bradley and P. D. Townsend, *J. Phys. D: Appl. Phys.*, 1987, **20**, 1367.

54 H. Goktas, X. Wang, N. D. Boscher, S. Torosian and K. K. Gleason, *J. Mater. Chem. C*, 2016, **4**, 3403–3414.

55 M. M. Wienk, M. Turbiez, J. Gilot and R. A. J. Janssen, *Adv. Mater.*, 2008, **20**, 2556–2560.

56 M. Gora, W. Krzywiec, J. Mieczkowski, E. C. Rodrigues Maia, G. Louarn, M. Zagorska and A. Pron, *Electrochim. Acta*, 2014, **144**, 211–220.

57 C. H. Woo, P. M. Beaujuge, T. W. Holcombe, O. P. Lee and J. M. J. Fréchet, *J. Am. Chem. Soc.*, 2010, **132**, 15547–15549.

58 R. Feng, N. Sato, T. Yasuda, H. Furuta and S. Shimizu, *Chem. Commun.*, 2020, **56**, 2975–2978.

59 K. Baba, G. Bengasi, D. El Assad, P. Grysan, E. Lentzen, K. Heinze, G. Frache and N. D. Boscher, *Eur. J. Org. Chem.*, 2019, **2019**, 2368–2375.

60 M. Stolte, S.-L. Suraru, P. Diemer, T. He, C. Burschka, U. Zschieschang, H. Klauk and F. Würthner, *Adv. Funct. Mater.*, 2016, **26**, 7415–7422.

61 J. Kesters, P. Verstappen, M. Kelchtermans, L. Lutsen, D. Vanderzande and W. Maes, *Adv. Energy Mater.*, 2015, **5**, 1500218.

62 B. Stadtmüller, S. Emmerich, D. Jungkenn, N. Haag, M. Rollinger, S. Eich, M. Maniraj, M. Aeschlimann, M. Cinchetti and S. Mathias, *Nat. Commun.*, 2019, **10**, 1470.

63 C. M. Mauck, P. E. Hartnett, Y.-L. Wu, C. E. Miller, T. J. Marks and M. R. Wasielewski, *Chem. Mater.*, 2017, **29**, 6810–6817.

64 C. M. Mauck, P. E. Hartnett, E. A. Margulies, L. Ma, C. E. Miller, G. C. Schatz, T. J. Marks and M. R. Wasielewski, *J. Am. Chem. Soc.*, 2016, **138**, 11749–11761.

65 D. W. Polak, M. T. do Casal, J. M. Toldo, X. Hu, G. Amoruso, O. Pomeranc, M. Heeney, M. Barbatti, M. N. R. Ashfold and T. A. A. Oliver, *Phys. Chem. Chem. Phys.*, 2022, **24**, 20138–20151.

66 R. Shivhare, G. J. Moore, A. Hofacker, S. Hutsch, Y. Zhong, M. Hambsch, T. Erdmann, A. Kiriy, S. C. B. Mannsfeld, F. Ortmann and N. Banerji, *Adv. Mater.*, 2022, **34**, 2101784.

67 A. M. Levine, G. He, G. Bu, P. Ramos, F. Wu, A. Soliman, J. Serrano, D. Pietraru, C. Chan, J. D. Batteas, M. Kowalczyk, S. J. Jang, B. L. Nannenga, M. Y. Sfeir, E. H. R. Tsai and A. B. Braunschweig, *J. Phys. Chem. C*, 2021, **125**, 12207–12213.

68 M. B. Smith and J. Michl, *Chem. Rev.*, 2010, **110**, 6891–6936.

69 P. E. Hartnett, E. A. Margulies, C. M. Mauck, S. A. Miller, Y. Wu, Y.-L. Wu, T. J. Marks and M. R. Wasielewski, *J. Phys. Chem. B*, 2016, **120**, 1357–1366.

70 L. Wang, W. Jiang, S. Guo, S. Wang, M. Zhang, Z. Liu, G. Wang, Y. Miao, L. Yan, J.-Y. Shao, Y.-W. Zhong, Z. Liu, D. Zhang, H. Fu and J. Yao, *Chem. Sci.*, 2022, **13**, 13907–13913.

71 A. C. Rosenfeldt, B. Göhler and H. Zacharias, *J. Chem. Phys.*, 2010, **133**, 234704.

72 T. Wang and W.-L. Chan, *J. Phys. Chem. Lett.*, 2014, **5**, 1812–1818.

73 J. Li, H. Cao, Z. Zhang, S. Liu and Y. Xia, *Photonics*, 2022, **9**, 689.

74 R. Tautz, E. Da Como, T. Limmer, J. Feldmann, H.-J. Egelhaaf, E. von Hauff, V. Lemaur, D. Beljonne, S. Yilmaz, I. Dumsch, S. Allard and U. Scherf, *Nat. Commun.*, 2012, **3**, 970.

75 B. S. Rolczynski, J. M. Szarko, H. J. Son, Y. Liang, L. Yu and L. X. Chen, *J. Am. Chem. Soc.*, 2012, **134**, 4142–4152.

76 M. Mirabedin, H. Vergnes, N. Caussé, C. Vahlas and B. Caussat, *Appl. Surf. Sci.*, 2021, **554**, 149501.

77 F. Muralter, A. M. Coclite and K. K. S. Lau, *Adv. Electron. Mater.*, 2021, **7**, 2000871.

78 S. Kaviani, M. Mohammadi Ghaleni, E. Tavakoli and S. Nejati, *ACS Appl. Polym. Mater.*, 2019, **1**, 552–560.

79 S. Stas, S. Sergeyev and Y. Geerts, *Tetrahedron*, 2010, **66**, 1837–1845.

80 A. B. Tamayo, M. Tantiwiwat, B. Walker and T.-Q. Nguyen, *J. Phys. Chem. C*, 2008, **112**, 15543–15552.